

Article

Effects of L-PBF Scanning Strategy and Sloping Angle on the Process Properties of TC11 Titanium Alloy

Xuben Lu ^{1,2}, Chang Shu ³, Zhiyu Zheng ^{1,2}, Xuedao Shu ^{1,2,*} , Siyuan Chen ^{1,2}, Khamis Essa ³ , Zixuan Li ^{1,2} and Haijie Xu ^{1,2}

¹ Faculty of Mechanical Engineering and Mechanics, Ningbo University, Ningbo 315211, China; 2111081154@nbu.edu.cn (X.L.); zzy253533237@gmail.com (Z.Z.); 2201090012@nbu.edu.cn (S.C.); lizixuan@nbu.edu.cn (Z.L.); xuhaijie@nbu.edu.cn (H.X.)

² Zhejiang Key Laboratory of Part Rolling Forming, Ningbo University, Ningbo 315211, China

³ Department of Mechanical Engineering, University of Birmingham, Birmingham B15 2TT, UK; cxs176@student.bham.ac.uk (C.S.); k.e.a.essa@bham.ac.uk (K.E.)

* Correspondence: shuxuedao@nbu.edu.cn

Abstract: TC11 titanium alloy is widely used in aerospace. To investigate the production of TC11 titanium alloy parts of high quality and performance, this paper adopts the Laser powder bed fusion (L-PBF) technique to prepare TC11 alloy specimens. We analyze in detail the effects of scanning strategy and forming angle on the forming quality and performance of TC11 alloy through a combination of theory and experiment. The results show that the upper surface quality of the strip-scanned molded parts is the highest, and the upper surface quality is better than that of the side surface under different scanning strategies. The fusion channel lap and surface adhesion powder were the main factors affecting the surface roughness. With increases in the forming angle, the surface roughness of the overhanging surface gradually decreases and the hardness gradually increases. The surface quality and hardness of the specimen are optimal when the forming angle is 90°. The research results provide the theoretical basis and technical support for L-PBF forming of TC11 titanium alloy parts.

Keywords: scanning strategy; forming angle; TC11 titanium alloy; forming quality



Citation: Lu, X.; Shu, C.; Zheng, Z.; Shu, X.; Chen, S.; Essa, K.; Li, Z.; Xu, H. Effects of L-PBF Scanning Strategy and Sloping Angle on the Process Properties of TC11 Titanium Alloy. *Metals* **2023**, *13*, 983. <https://doi.org/10.3390/met13050983>

Academic Editors: Vera Popovich and Thorsten Becker

Received: 24 April 2023

Revised: 9 May 2023

Accepted: 17 May 2023

Published: 19 May 2023



Copyright: © 2023 by the authors. Licensee MDPI, Basel, Switzerland. This article is an open access article distributed under the terms and conditions of the Creative Commons Attribution (CC BY) license (<https://creativecommons.org/licenses/by/4.0/>).

1. Introduction

Laser powder bed fusion (L-PBF) is a sophisticated additive manufacturing technique that utilizes a digital model file of a three-dimensional slice of a part as the foundation for sequentially melting fine metal powder particles, layer by layer, with a high-energy laser beam. This process results in the solidification of the melted powder, thereby producing a formed part [1–3]. L-PBF technology is extensively employed in the aerospace, defense, and biomedical sectors, owing to its rapid forming speed, absence of tooling requirements, net forming capability, high precision, high density, and the ability to fabricate intricate components [4].

Titanium alloys are widely favored due to their exceptional properties, such as high specific strength, superior corrosion and high-temperature resistance, and excellent fatigue resistance [5,6]. However, the traditional machining process for these alloys poses several challenges, including high cutting temperatures, strong chemical activity, and severe tool sticking, making it particularly difficult to manufacture complex parts by cutting. As aerospace equipment requirements increasingly demand intricate, high-performance designs, traditional manufacturing methods such as casting, forging, welding, and machining have become inadequate [7,8]. At present, the complex and high-precision titanium alloy parts formed by L-PBF can not only solve the problem that titanium alloy is difficult to process, but also ensure that the formed parts have good comprehensive properties and

fully utilize the excellent properties of titanium alloy. This processing method has become a new direction for future development and has broad application prospects [9,10].

The quality and performance of the printed parts in laser powder bed fusion are directly affected by the process parameters [11], making the selection of these parameters of utmost importance. Currently, many researchers are investigating the impact of L-PBF process parameters on forming quality. Xinyue C et al. [12] studied the effects of L-PBF layer thickness, preheating temperature and scanning strategy on Ti-6Al-4V alloy. The results show that by manipulating the thermal gradient and heat accumulation in the L-PBF process, the residual stress changes from a non-uniform distribution with a local value of up to 600 MPa to a relatively flat distribution below 100 MPa, which provides an effective method for reducing in situ stress. Jca B et al. [13] controlled the phase structure and phase transition temperature of NiTi alloy by changing the process parameters of L-PBF, which provided a theoretical and experimental basis for improving the comprehensive performance of NiTi alloy. Zhongpeng Z et al. [14] studied the influence of selective laser melting scanning strategy on the anisotropy of Ti6Al4 V material surface morphology, microstructure, microhardness, quasi-static and dynamic mechanical properties, concluding that the scanning strategy can affect the comprehensive performance of the parts. Sadali et al. [15] studied the effect of SLM scanning speed on the forming quality of TC4 parts and found that a scanning speed of 775 mm/s produced good surface morphology and microstructure. Using the controlled variable method, Yang, Lijun et al. [16] investigated the effect of laser power on TC4 parts and found that high laser power resulted in overburning or spheroidization, while low laser power led to decreased densities due to incomplete melting. Wo'zniak et al. [17] observed the surface morphology of SLM-prepared samples and found that laser power and scanning speed significantly affected the obtained material's high corrosion resistance, full density, and lack of defects. Greco et al. [18] investigated the effect of SLM parameters on forming quality and found that increasing laser power for a constant input line energy density led to a decrease in surface roughness perpendicular to the stacking direction and an increase in relative density. However, current research on L-PBF process parameters primarily focuses on laser power, scanning speed, and scanning pitch, with limited studies on scanning strategies and forming angles.

Different scanning strategies and forming angles have a significant impact on the surface quality, dimensional accuracy, and forming time of parts [19]. The $\alpha + \beta$ dual phase titanium alloy combines the excellent properties of α and β titanium alloys, which are high strength and good thermal stability. As a result, $\alpha + \beta$ titanium dual phase titanium alloy constitutes more than 50% of the overall use of titanium alloys, mainly represented by TC4, TC11 and so on [20]. Since the concept of TC4 titanium alloy as was first proposed as a material in additive manufacturing, there have been relatively many studies on the additive manufacturing of TC4 [21]. TC11 titanium alloy has wide application prospects as the main raw material for manufacturing engines, turbine blades, missiles and other products in the aerospace field. However, there are few studies on L-PBF forming of TC11 titanium alloy. Therefore, this research aimed to prepare samples of TC11 titanium alloy using the L-PBF process under various scanning strategies and forming angles. The micro-morphology of the samples was observed, and changes in microhardness and surface roughness were analyzed to provide a theoretical foundation and technical guidance for producing high-quality and high-performance TC11 titanium alloy parts.

2. Experimental Materials and Methods

2.1. Experimental Materials

TC11 titanium alloy powder was prepared by the aerosol method. EDS was used for component detection, and its chemical composition is shown in Table 1; the main component was titanium. The microstructure of TC11 titanium alloy powder photographed by SEM is shown in Figure 1a. The powder generally presents an approximate regular spherical shape with a smooth surface, an absence of other impurities, and good wettability. The Winner2000 laser particle size analyzer was used to measure the particle size of TC11

powder. The particle size distribution is shown in Figure 1b. The particle size of the powder was mostly distributed in the range of 15~53 μm with a Gaussian distribution, which met the printing requirements of the equipment.

Table 1. Chemical composition of TC11 powder (mass fraction %).

Element	Ti	Zr	Al	Fe	Mo	Si	C	H	N	O
Mass fraction (%)	88.05	1.43	6.44	0.182	3.52	0.255	0.014	0.0033	0.001	0.096

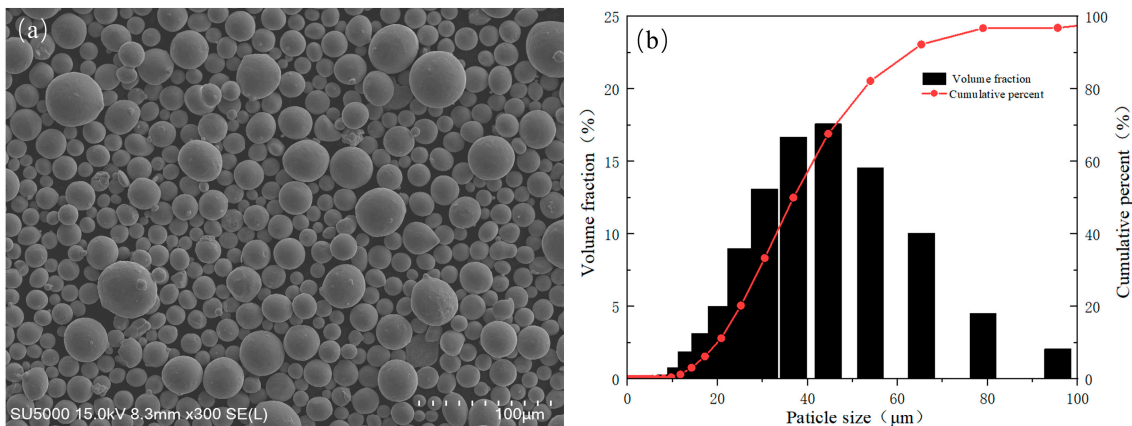


Figure 1. (a) SEM microscopic morphology, and (b) particle size distribution.

2.2. Experimental Equipment

The experiment utilized the HBD-150 3D printing equipment manufactured by Hanbang Lianhang Technology Co., LTD. (Shanghai, China). This equipment has a maximum forming size of $\phi 159 \times 100$ mm, a maximum laser power of 500 W, a maximum scanning speed of 10,000 mm/s, a printing layer thickness of 10–40 μm , and a laser diameter of 60 μm . Surface roughness was measured using the LSM900 confocal microscope (Carl Zeiss AG, Oberkochen, Germany), which provides accurate three-dimensional imaging and analysis of various materials such as nanomaterials, metals, and polymers. The maximum laser wavelength of LSM900 is up to 640 nm, and it can achieve scanning magnification ranging from 0.5 to 40 times. Microhardness measurements were conducted using the VH-1102 microhardness tester (Wilson, New York, NY, USA), which has a pressure range of 100~2000 g, a holding time of 5~99 s, and a test depth of 0~130 μm .

2.3. Experimental Method

The $8 \times 8 \times 8$ mm block specimen model was created using SolidWorks software (version 2016, Dassault Systemes, Paris, France). To investigate the effects of scanning strategy, a scanning strategy as shown in Figure 2 was designed. All three scanning strategies utilized a layer-by-layer rotation of 67° for the interlayer scan lines. For the intra-layer scan, the strip strategy divided the 2D cross-section into three regions, which were scanned in an adjacent region order using a simple back-and-forth alternating scan within each region, with the vectors of adjacent regions parallel to each other. The linear scanning strategy employed a straightforward “back and forth” scanning mode throughout the entire plane. Lastly, the chessboard scanning strategy divided each constructed slice into four small regions resembling a chessboard pattern and selectively melted each region in random order using a simple alternating scanning vector, with paths in adjacent regions perpendicular to each other [22]. Furthermore, the plane perpendicular to the forming direction is referred to as the forming surface, whereas the plane parallel to the forming direction is known as the side surface.

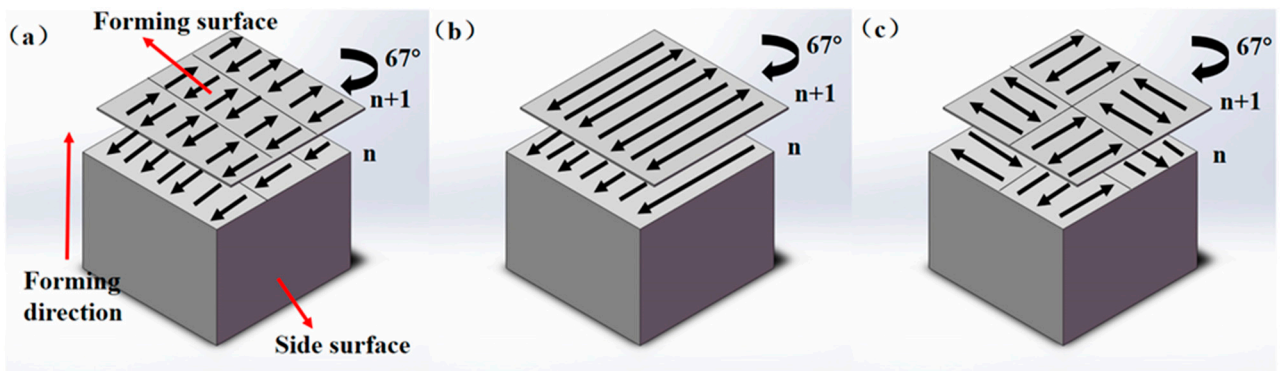


Figure 2. Schematic diagram of scanning strategy forming: (a) strip, (b) line, and (c) checkerboard.

The forming angle, which is also known as the sloping angle, refers to the angle between the side of the formed specimen and the substrate, whose side is also known as the overhanging surface. The plane perpendicular to the forming direction is called the front surface. If the sloping angle is too small, the overhanging surface tilts to a greater extent, and the specimen is prone to deformation such as warpage deformation, cracking and other phenomena [23]. Therefore, in the actual forming process, support is usually added to the part where the tilt angle is less than 45° . With complex parts in the actual printing process, the angle is usually between 45° and 90° . In order to study the effect of forming angle, 45° , 60° , 75° , and 90° tilt angles were selected for specimen printing as a basis for exploring the best placement of complex structural parts, as shown in Figure 3.

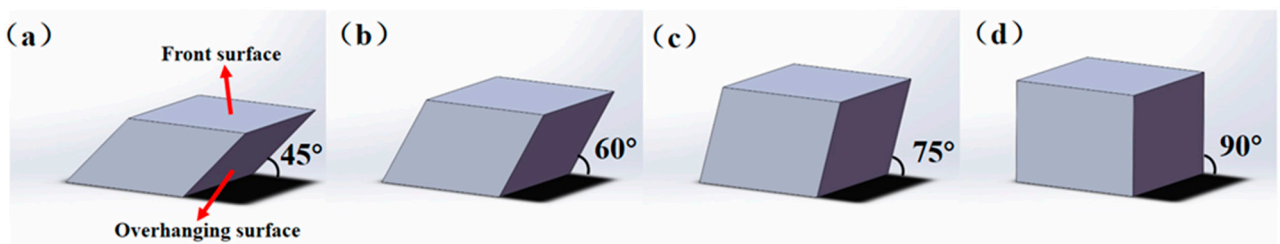


Figure 3. Schematic diagram of forming angle: (a) 45° , (b) 60° , (c) 75° , and (d) 90° .

During the forming process, titanium alloy was utilized as the substrate material, and to maintain the oxygen content below 500 ppm, an inert gas, argon, was introduced into the forming chamber. After drying the powder, the following parameters were set for printing the TC11 titanium alloy: a laser power of 170 W, a scanning speed of 1100 mm/s, a scanning interval of 0.1 mm, and a forming layer thickness of 30 μm . The formed sample is presented in Figure 4. Surface roughness was evaluated using the laser confocal microscope LMS900, with 5 measurements per surface, 2.5 mm measurement length, and 1 μm measurement interval. The region method was used to obtain data through a planar three-dimensional surface structure, which was characterized by arithmetic average height (S_a) and root mean square height (S_q). S_a refers to the absolute average of the height difference between the surface and the center line, which is used to describe the overall roughness. The larger the value, the higher the surface roughness. S_q is the average of the square sum of the height difference between the peak and the valley in all the calculated lengths, which is used to describe the degree of fluctuation in the surface, and can fully reflect the complexity and variation of the surface. Both are important indicators of surface roughness. Microhardness was examined using the VH-1102 microhardness tester, with a chosen load of 1 kg and a loading time of 60 s. Five points were arbitrarily chosen from the measured plane, and the average value was recorded.

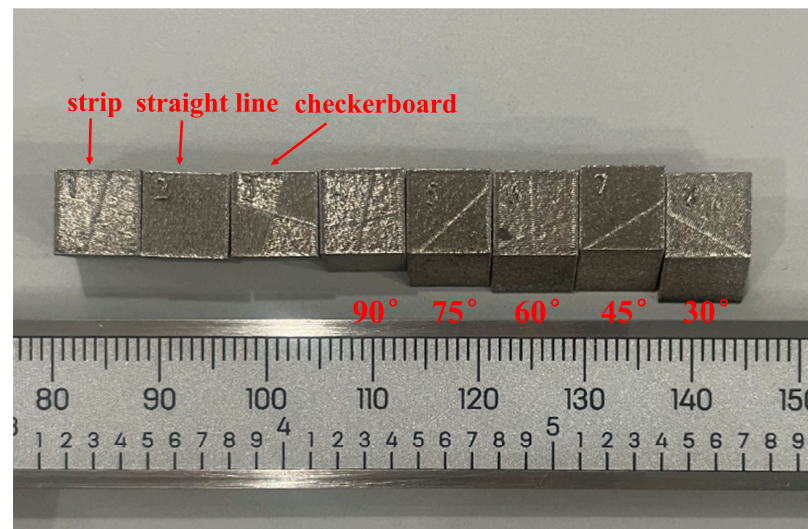


Figure 4. Block specimens.

3. Results and Analysis

3.1. Effect of Scanning Strategy on Surface Morphology and Roughness

Figure 5 shows the shape of the forming surface and the roughness values of the block specimens under different scanning strategies. Figure 6 shows the height change in the line profile of the forming surface under different scanning strategies. The curve is generally stable, with individual peaks appearing, and the change is consistent with the roughness value. Comparing the surface morphology of the three scanning strategies, clear scanning trajectories can be seen, and it can also be observed that the weld overlap presents a relatively dense state. There are no obvious crater phenomena caused by ablation and no obvious cracks or holes. This is due to the “back and forth” scanning mode adopted by the three strategies, which ensures that the flow direction of the adjacent molten pool is strictly opposite, which ensures that the gap generated by the flow of the adjacent molten pool can be filled, thereby ensuring the forming quality. The main defect is the spheroidal phenomenon caused by the molten powder splashing onto the melt channel. Compared with the striping and checkerboard strategies, the sputtering phenomenon of samples under the linear strategy is more obvious, and some fine micro-cracks can be observed in some areas between the channels. This is because the linear laser thread is longer, and the continuous non-partitioned laser scanning leads to the molten pool being in continuous heat transfer mode. Under the condition of inevitable solidification and contraction of the molten pool, continuous heat transfer helps to restrain crack propagation [24], but this condition is also prone to generate energy accumulation, resulting in powder spatter. Comparing the roughness values of the three scanning strategies, the overall change is not obvious. The roughness value of the striping scanning strategy is small and the surface is relatively flat, whereas the value for checkerboard scanning strategy is large. This is because the checkerboard strategy is a type of zoned scanning strategy. During processing, the high energy laser beam divides the melting zone of the powder bed into several small zones and gradually melts it step by step in a certain order, which results in the thermal stress generated by melting and solidification being evenly distributed at the boundary of the zone, thus reducing the tendency for concentrated release of residual stress and suppressing crack growth [25]. However, the division of regions leads to more lap connections between regions, and there are more obvious lap connections, resulting in an uneven surface and increased overall roughness.

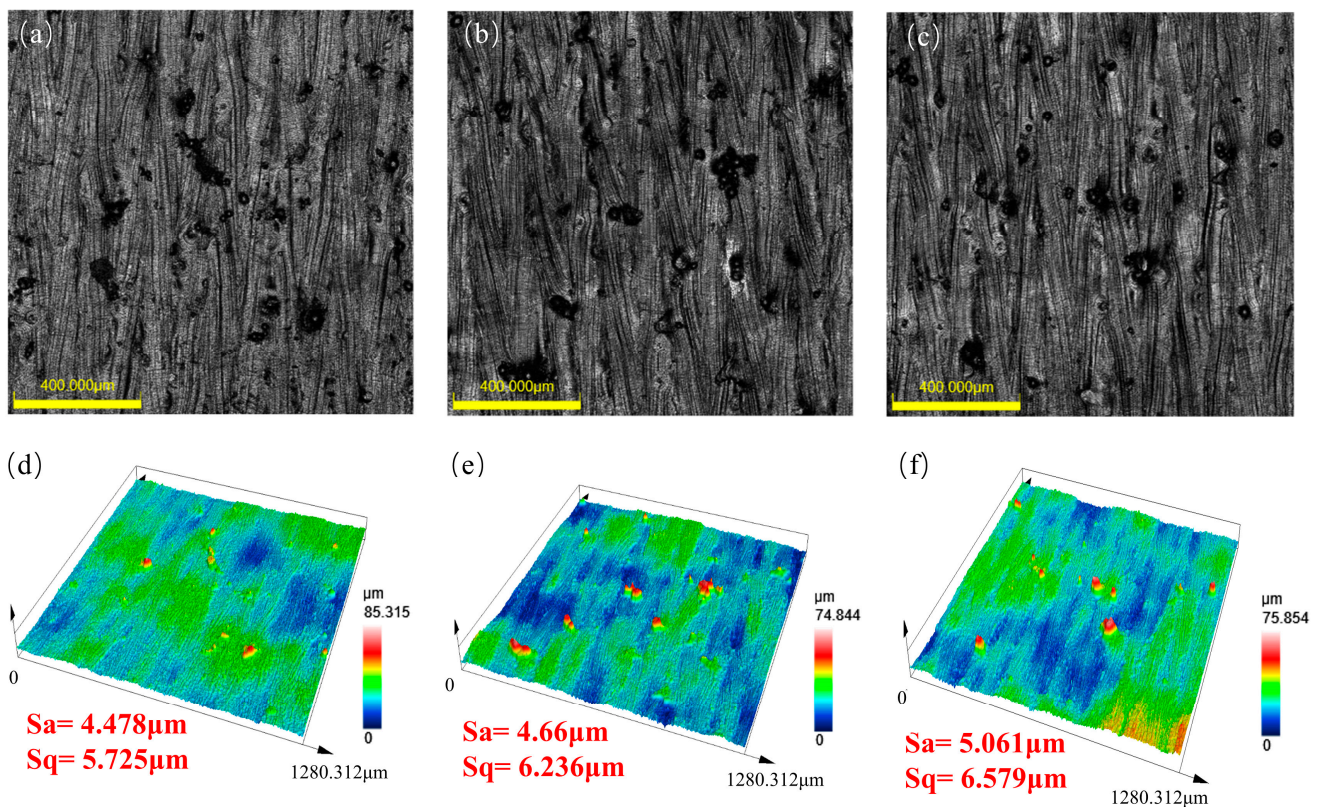


Figure 5. Frontal morphology and roughness with different scanning strategies: (a,d) strip; (b,e) straight line; and (c,f) checkerboard.

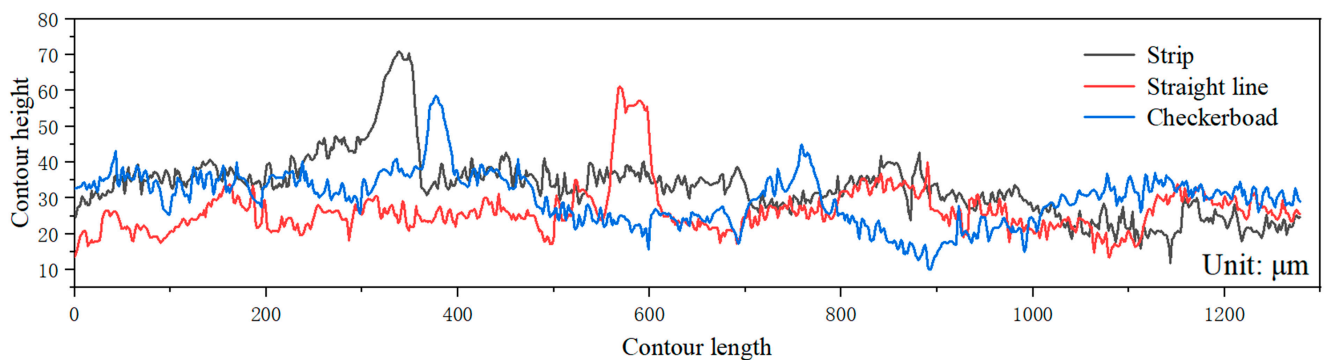


Figure 6. The line profile height change in the forming surface under different scanning strategies.

The side surface morphology and side roughness of the formed parts are shown in Figure 7. Because the angle between the middle layer and the layer rotates 67 degrees during the sample forming process, the elliptic welds overlap with each other, resulting in a certain unleveling phenomenon on the side of the sample formed under the three scanning strategies. Additionally, the laser remains for a while when it reaches the edge of the forming surface, so the powder melting time at the edge is longer than in the middle of the molten pool, resulting in serious powder adsorption phenomenon. In addition, the powder is fused through heat conduction, and the energy decreases in the process of transfer. Partial powder also appears due to incomplete melting, which affects the forming quality of the side surface [26]. Figure 8 shows the height change in the line profile on the side. Compared with the front, the curve has obvious changes, with a large number of peaks and troughs, and the distance between the peaks and troughs is further widened. The results of roughness measurement show that the side roughness of the samples formed

under the three scanning strategies of strip scanning, straight scanning and checkerboard scanning is at the same level and is higher than that of the front surface.

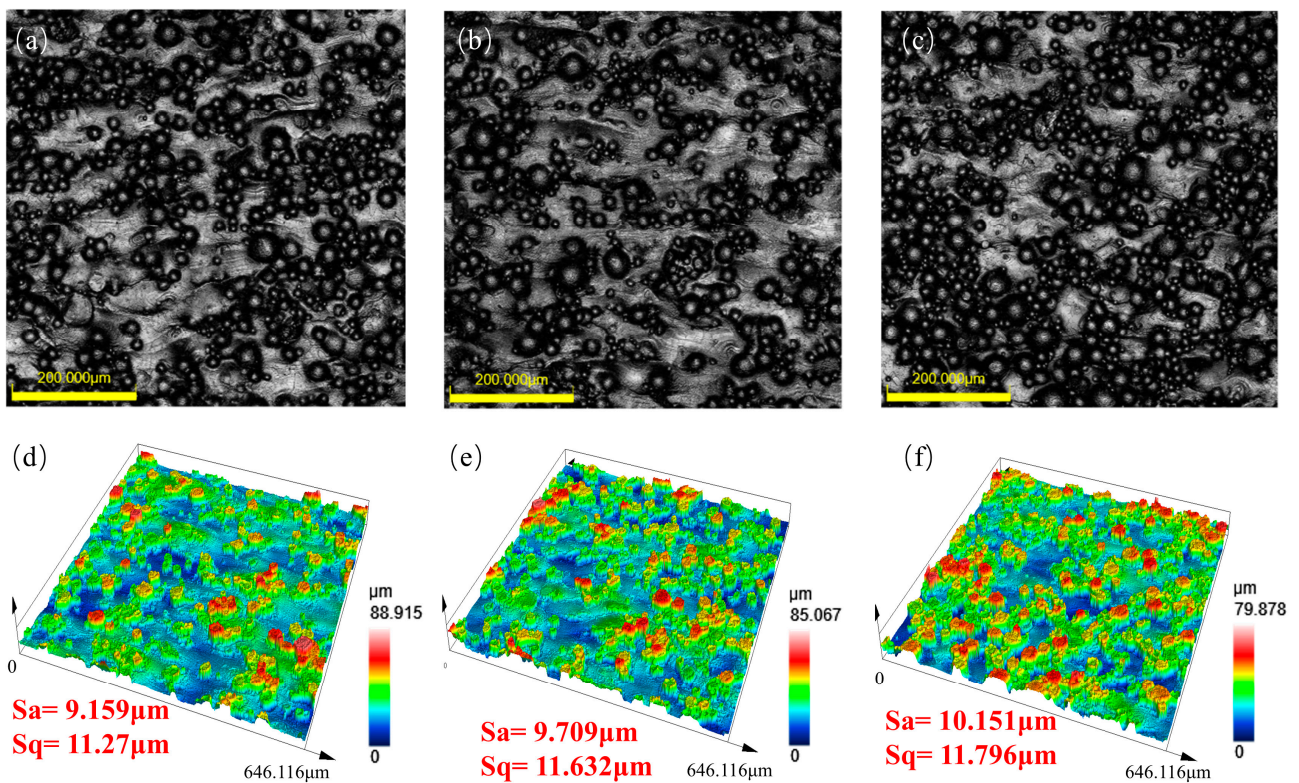


Figure 7. Side morphology and roughness with different scanning strategies: (a,d) strip; (b,e) straight line; and (c,f) checkerboard.

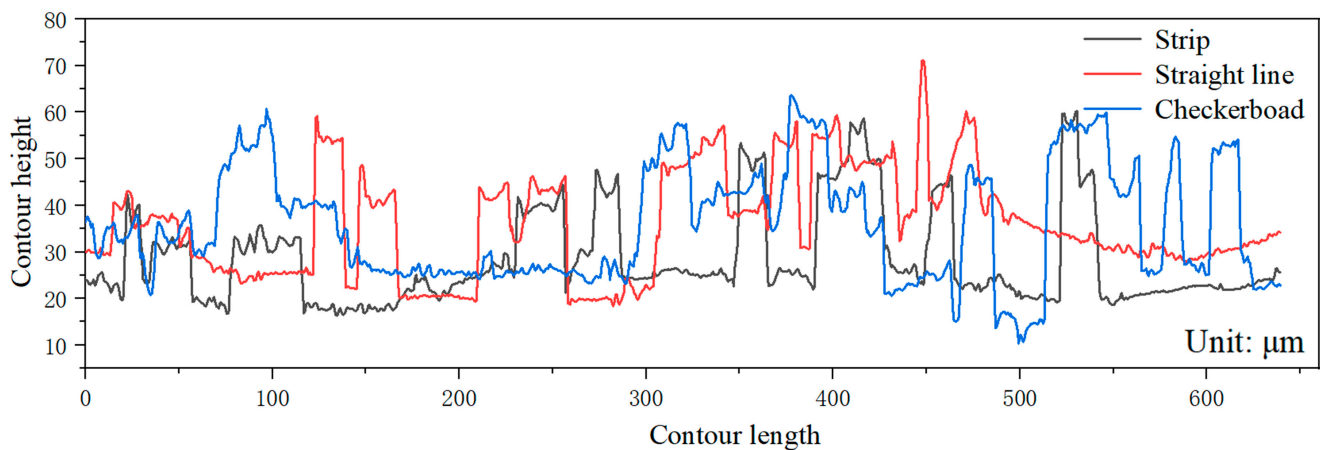


Figure 8. The height change in the side line profile under different scanning strategies.

3.2. Effect of Scanning Strategy on Microhardness

Table 2 shows the average microhardness values under three scanning strategies. The microhardness of linear scanning is greater than that of the other two scanning strategies, mainly because the checkerboard scanning strategy and strip scanning strategy are both partitioned scanning strategies, and the scanning line length is smaller than that of single-fill linear scanning. Due to the short scanning line length, the scanning time of the two adjacent scanning lines is relatively short when laser is applied to the powder surface. The temperature gradient in the scanned area decreases, and the cooling rate decreases, so that the overall temperature of the forming surface is higher and the growth time of the grains

is sufficient. As a result, the grains are coarse and the number of grain boundaries of the whole sample is reduced. When subjected to external forces, the obstacle to dislocation movement is reduced and the hardness is only low [27]. Therefore, the microhardness of the checkerboard and strip scanning samples was lower than that of linear scanning, and the value for checkerboard scanning was greater than that of strip scanning. After laser scanning a region, the adjacent region can be preheated by heat conduction. The preheating times are longer so that the overall temperature gradient is smaller and the grain is coarser, resulting in a decrease in hardness. The Archimedes drainage method was used to measure the density of the samples under different scanning strategies. The samples were ground and polished for metallographic observation. The results are shown in Figure 9. The density of the samples reached more than 98.67 %, indicating that the overall forming quality of the samples was good, and that selection of the laser parameters was reasonable. The density of the straight line scanning sample was higher than that of the other two, and the density of the chessboard scanning sample was the lowest. The corresponding metallographic diagram also shows that there are certain pores and micropores in the chessboard scanning sample. The overall surfaces of the straight line and the strip samples are smooth, without cracks or large pores but with individual tiny pores. This is due to the excessive overlap between the scan partitions of the chessboard sample, which easily leads to defects such as pores, thereby reducing its hardness.

Table 2. Microhardness under different scanning strategies.

Scanning Strategy	Microhardness (HV)					Average Value
	1	2	3	4	5	
Strip scanning	365.7	374.8	370.7	364.9	377.2	370.7 ± 23.54
Straight line scanning	378.8	390.4	381.6	379.7	388.5	383.8 ± 22.46
Checkerboard scanning	370.5	362.4	364.8	355.6	368.7	364.4 ± 27.46

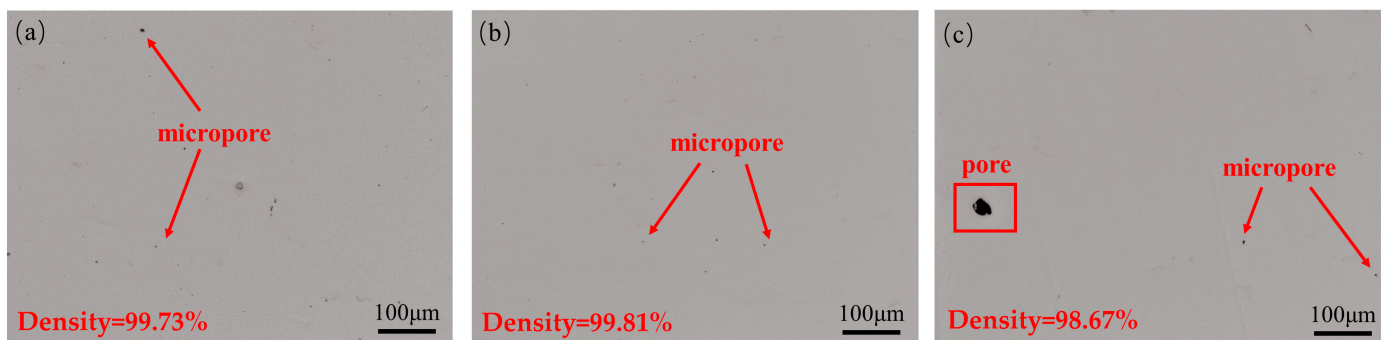


Figure 9. Density and metallographic diagram under different scanning strategies: (a) strip; (b) straight line; and (c) checkerboard.

3.3. Effect of Forming Angle

Figures 10 and 12a, show changes in the roughness of the specimen's frontal surface and overhanging surface with different overhang angles. It can be seen that the roughness values of the frontal surface and overhanging surface are affected by the overhang angle. The front roughness is lower than that of the overhanging surface on the whole, and a complete banded weld can be observed, which is generally smooth and locally raised, mainly due to the spheroidization phenomenon caused by the splashing powder. The overhanging surface roughness changes greatly, the surface is uneven, and even folds appear. There are many granular bulges, and the bulges become more serious with decreases in the overhang angle. Figure 11 shows the height variation diagram of the line contour at the overhang angles of 90° and 45° . It can be clearly observed that, on the whole, the 45° curve is higher than the 90° curve and that the distance between the crest and trough also further

increases. This indicates that the overhang angle is the key factor affecting the surface quality of the overhanging surface, and the smaller the overhang angle, the worse the surface quality. Due to the technological characteristics of L-PBF, there is a “step effect” on the overhanging surface, and the effect is more obvious when the overhang angle is larger, which is conducive to powder adhesion. At the same time, an increase in the overhang angle also leads to an increase in the overhang area, which is supported by powder, and the laser energy cannot be transferred in time. The energy concentration causes the volume of the molten pool shrink, resulting in an increase in unit energy density [28]. The metal powder particles under the laser sintered layer are easily melted, resulting in a serious powder adhesion phenomenon on the overhanging surface, which increases the surface roughness. The “step effect” is shown in Figure 12b.

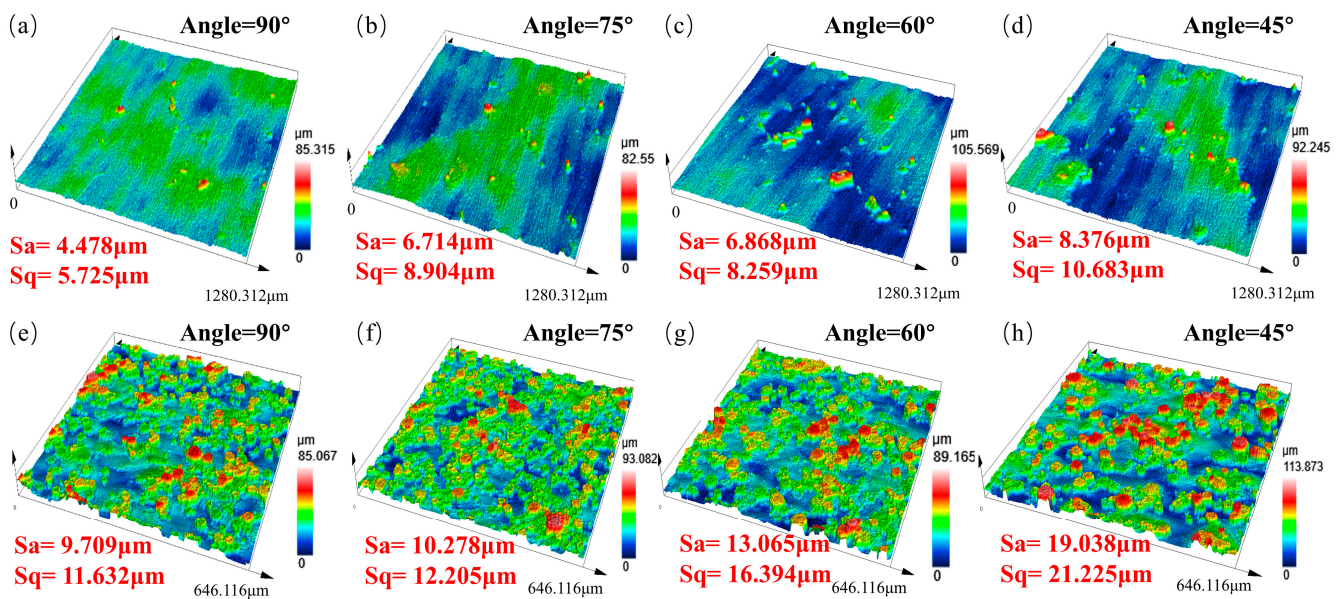


Figure 10. Roughness of the front (a–d) and overhanging, (e–h) surfaces of samples at different overhang angles.

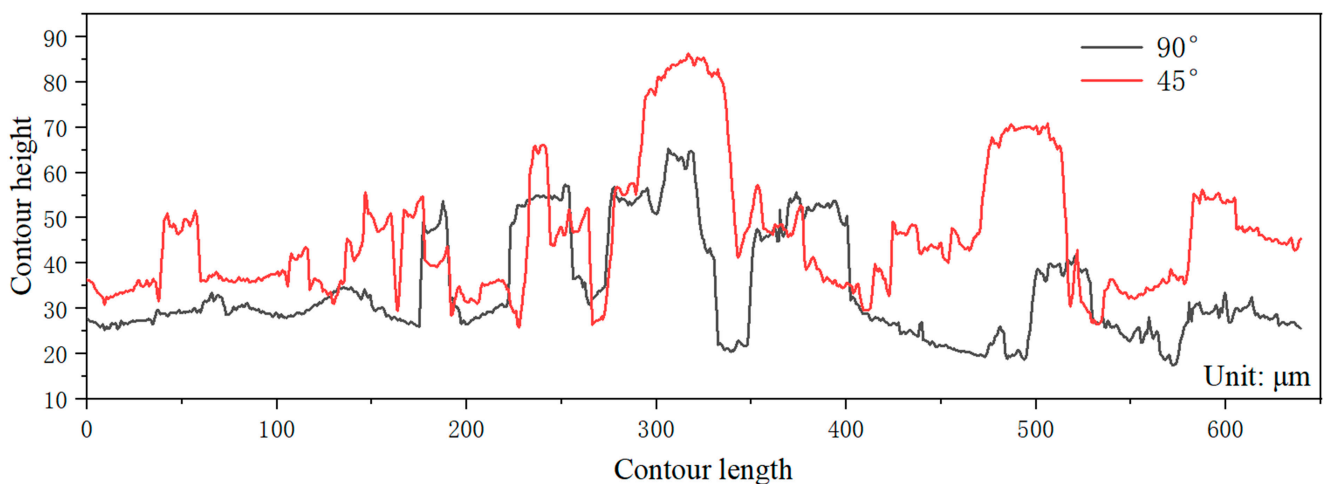


Figure 11. Line profile height variation.

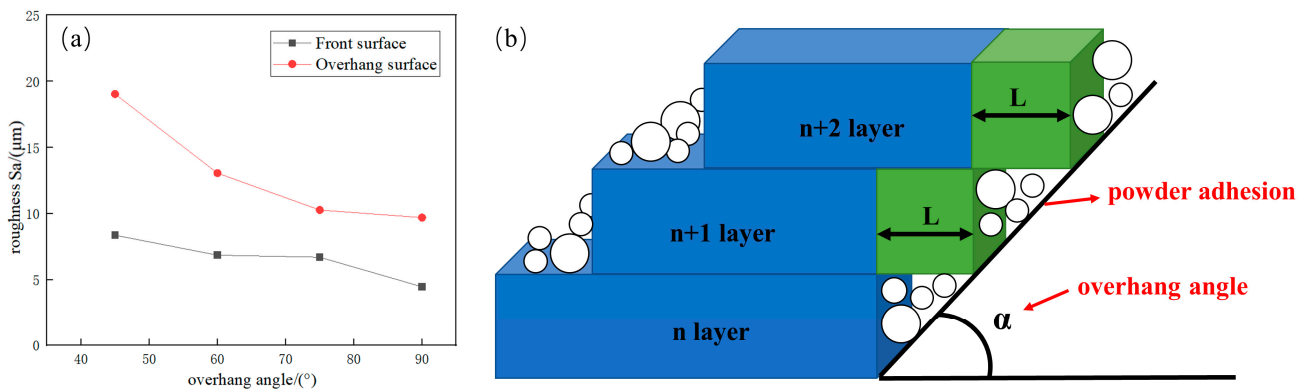


Figure 12. (a) Schematic diagram of sample roughness change; (b) schematic diagram of “step effect”.

3.4. Effect of Sloping Angle on Microhardness of Sample

Figure 13 shows the microhardness of the front and overhanging surface of the sample under different forming angles. It can be observed that different forming angles have little influence on the front microhardness but have great influence on the overhanging surface. With increases in the forming angle, the microhardness shows an increasing trend. This is because the forming quality of the overhanging surface is affected by the overhang length (L) between two adjacent layers. When the laser is applied to part L, the forming process is suspended over the metal powder, and the thermal conductivity of the support area of the powder is only 1/100 of that of the corresponding formed body [29]. The low thermal conductivity leads to the timely transmission of thermal stress. Coupled with the effect of structural stress and residual stress, plastic deformation occurs on the overhanging surface. The melted powder sinks into the powder layer below due to the action of capillary forces and gravity [30], resulting in poorer forming quality. As shown in Figure 14, when the forming angle is smaller, the overhang length (L) is longer, and $L_1 < L_2 < L_3 < L_4$. The greater the amount of deformation subsidence, the larger the decrease in forming quality and hardness.

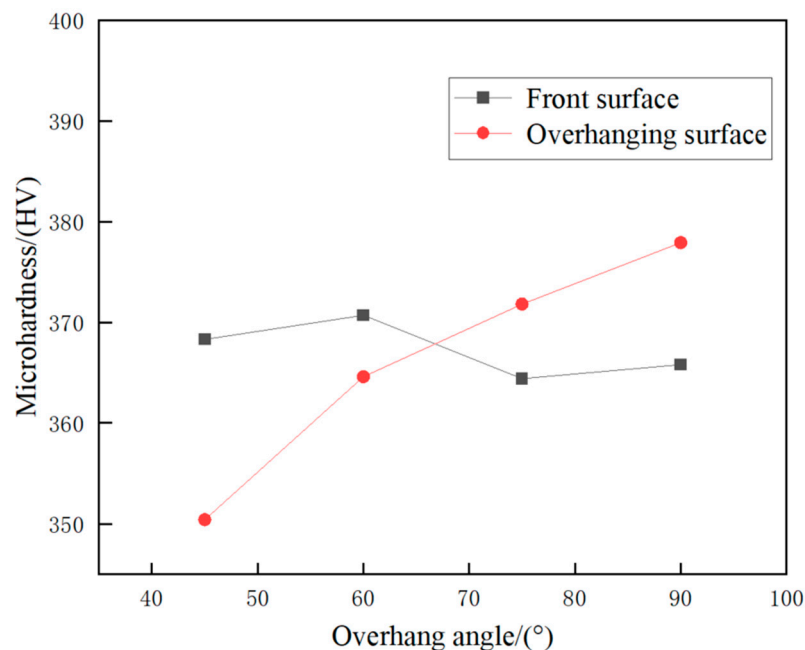


Figure 13. Microhardness of samples under different forming angles.

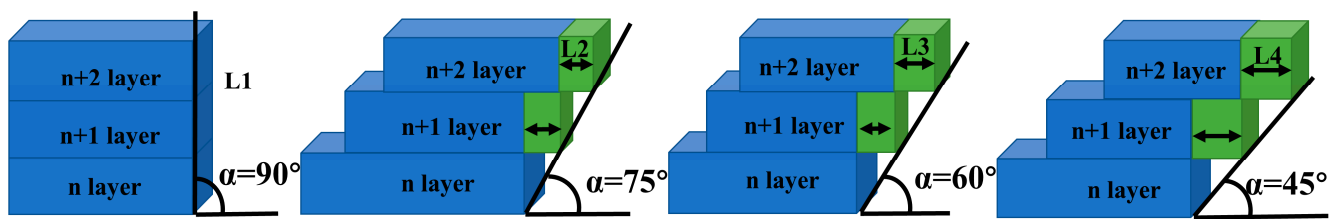


Figure 14. The overhang length change diagram.

In addition, it was found that the hardness of the side of a specimen formed with forming angle under 90° is higher than that of the front. This is because the front is the forming surface, the adjacent melting road is the “channel–channel” lap, the side is the deposition surface, and the adjacent melting road is the “layer–layer” lap. After the laser processes a layer, it needs to be paved with powder before processing the next layer, and the processed layer, therefore, has enough time to cool down. When processing the next layer, the temperature difference “layer to layer” is greater than that “channel to channel”, and the grain grows along the direction of the fastest heat dissipation, so the direction of grain growth is mostly vertical, resulting in the grain orientation on both sides of the weld boundary of the “layer to layer” lap being basically consistent [31]. As shown in Figure 15, the grain orientation on both sides of the weld is the same, and the microhardness increases when the weld is stressed more evenly, that is, the “channel–channel” lap is better than the “layer–layer” lap. When the forming angle changes, the lapping condition of the overhanging surface is between “channel–channel” lapping and “layer–layer” lapping [32]. Therefore, with decreases in the forming angle, the overhanging surface tends to the forming plane, and the higher the proportion of “layer–layer” bonding, the greater the microhardness of the sample.

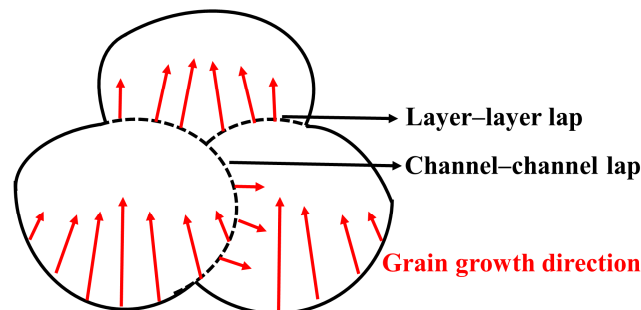


Figure 15. Grain growth direction diagram.

4. Conclusions

TC11 alloy samples were prepared by laser powder bed fusion technology. The effects of three scanning strategies including stripe, straight line and chessboard scanning, and the forming angle within $45\sim 90^\circ$ on the surface morphology, roughness and microhardness of the samples were studied. The following conclusions are obtained:

(1) The scanning strategy has an effect on the roughness of both the front and side of the sample. The front roughness is mainly affected by the overlap of the melt channel and the spheroidization caused by the powder splash. The linear strategy easily leads to the problem of energy accumulation, and the powder splash phenomenon is obvious. The strip and chessboard strategies are types of partition scanning. Using these strategies, there are more melt channel overlaps on the front surface, leading to an uneven surface. The roughness of the side is generally higher than that of the front surface. The main reason is that the melting time of the powder at the edge is longer than that of the powder in the middle of the molten pool, resulting in serious powder adsorption. A relatively low level of roughness was obtained using the strip scanning strategy.

(2) The microhardness of samples formed with different scanning strategies is different. The linear scanning strategy has the highest hardness, and the chessboard strategy has lower hardness. The reason is that under the partition scanning strategy, the scanning line length is different, which leads to changes in the temperature gradient in the scanning area, thus affecting the growth of grains. Under partition scanning, the temperature gradient decreases, the cooling rate decreases, the grain growth is coarse, the number of grain boundaries is small, the dislocation movement obstruction is reduced, and the hardness is low. The density of the checkerboard sample is low, and there are some defects such as a small number of pores inside, which further affects the hardness.

(3) The forming angle has little effect on the front roughness of the sample, but has a great influence on the overhanging surface. As the forming angle becomes larger, the roughness of the overhanging surface gradually becomes smaller. The main reason is the step effect of the overhanging surface. The smaller the forming angle, the more obvious the step effect, the more serious the powder adhesion and the greater the roughness.

(4) The forming angle has a significant influence on the microhardness of the overhanging surface of the sample. The main reason is that the thermal conductivity of the powder and the solid changes. When the forming angle decreases, the longer the drape length L , the larger the forming area in the powder layer, the greater the deformation subsidence, the worse the forming quality, and the lower the hardness. In addition, the grain growth direction under the 'channel-channel' lap is basically the same, and the force is more uniform. The hardness of the 'channel-channel' lap is greater than that of the 'layer-layer' lap. With a decrease in forming angle, the proportion of 'channel-channel' lap joints on the overhanging surface decreases, and the proportion of 'layer-layer' lap joints increases, resulting in decreased microhardness of the sample.

Author Contributions: X.L.: Write manuscripts and contribute significantly to research acquisition, experimental protocols, charting, data analysis and data interpretation. C.S.: Manuscript writing, Experimental data management and data analysis. Z.Z.: Experimental verification, data collection and interpretation of data. X.S.: Manuscript writing and finalizing the version to be published, and project and funding support. S.C.: Literature search, experimental scheme design and data collection. K.E.: Article content concept and design. Z.L.: Chart design, visualization of the experimental data and analyzing the data. H.X.: Manuscript writing, research design, experimental exploration, experiment supervision. All authors have read and agreed to the published version of the manuscript.

Funding: This study was funded by the National Natural Science Foundation of China (grant number: 51975301), the Natural Science Foundation of Zhejiang, China (grant number: LZ22E050002), and the Major Project of Science and Technology Innovation 2025 in Ningbo City, China (grant number: 2022Z064).

Data Availability Statement: All relevant data are within the article.

Conflicts of Interest: The authors declare no conflict of interest.

References

1. Li, N.; Huang, S.; Zhang, G.; Qin, R.; Liu, W.; Xiong, H.; Shi, G.; Blackburn, J. Progress in Additive Manufacturing on New Materials: A Review. *J. Mater. Sci. Technol.* **2019**, *35*, 242–269. [[CrossRef](#)]
2. Yang, J.; Han, J.; Yu, H.; Yin, J.; Gao, M.; Wang, Z.; Zeng, X. Role of molten pool mode on formability, microstructure and mechanical properties of selective laser melted Ti-6Al-4V alloy. *Mater. Des.* **2016**, *110*, 558–570. [[CrossRef](#)]
3. Shahrubudin, N.; Chuan, L.T.; Ramlan, R. An Overview on 3D Printing Technology: Technological, Materials, and Applications. *Procedia Manuf.* **2019**, *35*, 1286–1296. [[CrossRef](#)]
4. Gu, D.D.; Zhang, H.M.; Chen, H.Y.; Zhang, H.; Xi, L. Laser Additive Manufacturing of High-Performance Metallic Aerospace Components. *Chin. J. Lasers* **2020**, *47*, 32–55.
5. Morsi, K. Review: Titanium-titanium boride composites. *J. Mater. Sci.* **2019**, *54*, 6753–6771. [[CrossRef](#)]
6. Tshephe, T.S.; Akinwamide, S.O.; Olevsky, E.; Olubambi, P.A. Additive manufacturing of titanium-based alloys- A review of methods, properties, challenges, and prospects. *Heliyon* **2022**, *8*, e09041. [[CrossRef](#)]
7. Rahulan, N.; Sharma, S.S.; Rakesh, N.; Sambhu, R. A short review on mechanical properties of SLM titanium alloys based on recent research works. *Mater. Today Proc.* **2022**, *56*, A7–A12. [[CrossRef](#)]

8. Li, H.L.; Jia, D.C.; Yang, Z.H.; Duan, X.M.; Cai, D.L.; Zhou, Y. Research progress on selective laser melting 3D printing of titanium alloys and titanium matrix composites. *Mater. Sci. Technol.* **2019**, *27*, 1–15.
9. Pasang, T.; Budiman, A.S.; Wang, J.C.; Jiang, C.P.; Boyer, R.; Williams, J.; Misiolek, W.Z. Additive manufacturing of titanium alloys—Enabling re-manufacturing of aerospace and biomedical components. *Microelectron. Eng.* **2023**, *270*, 111935. [[CrossRef](#)]
10. Colombo-Pulgarín, J.C.; Biffi, C.A.; Vedani, M.; Celentano, D.; Sánchez-Egea, A.; Boccardo, A.D.; Ponthot, J.P. Beta Titanium Alloys Processed By Laser Powder Bed Fusion: A Review. *J. Mater. Eng. Perform.* **2021**, *30*, 6365–6388. [[CrossRef](#)]
11. Li, Y.; Liang, Z.; Sun, Z.; Chen, X. Study on the matching of TC4 alloy powder and SLM process parameters. *Inf. Rec. Mater.* **2022**, *23*, 10–13.
12. Chen, X.; Xie, X.; Wu, H.; Ji, X.; Shen, H.; Xue, M.; Wu, H.; Chao, Q.; Fan, G.; Liu, Q. In-situ control of residual stress and its distribution in a titanium alloy additively manufactured by laser powder bed fusion. *Mater. Charact.* **2023**, *28*, 112953. [[CrossRef](#)]
13. Chekotu, J.C.; Goodall, R.; Kinahan, D.; Brabazon, D. Control of Ni-Ti Phase Structure, Solid-State Transformation Temperatures and Enthalpies via Control of L-PBF Process Parameters. *Mater. Des.* **2022**, *218*, 110715. [[CrossRef](#)]
14. Zheng, Z.; Jin, X.; Bai, Y.; Yang, Y.; Ni, C.; Lu, W.F.; Wang, H. Microstructure and anisotropic mechanical properties of selective laser melted Ti6Al4V alloy under different scanning strategies. *Mater. Sci. Eng. A* **2022**, *831*, 142236. [[CrossRef](#)]
15. Sadali, M.F.; Hassan, M.Z.; Ahmad, F.; Yahaya, H.; Rasid, Z.A. Influence of selective laser melting scanning speed parameter on the surface morphology, surface roughness, and micropores for manufactured Ti6Al4V parts. *J. Mater. Res.* **2020**, *35*, 2025–2035. [[CrossRef](#)]
16. Yang, L.; Li, Y.; Zhu, Y.; Wen, P.; Shi, Z. Study on the Influence of Process Parameters on the Densification and Surface Hardness of TC4 Titanium Alloy Formed Parts by Selective Laser Melting. *Appl. Laser* **2022**, *42*, 55–62.
17. Woźniak, A.; Adamiak, M.; Ziębowicz, B. The surface morphology and electrochemical properties of pure titanium obtained by selective laser melting method. *Solid State Phenom.* **2020**, *308*, 21–32. [[CrossRef](#)]
18. Greco, S.; Gutzeit, K.; Hotz, H.; Kirsch, B.; Aurich, J.C. Selective laser melting (SLM) of AISI 316L—impact of laser power, layer thickness, and hatch spacing on roughness, density, and microhardness at constant input energy density. *Int. J. Adv. Manuf. Technol.* **2020**, *108*, 1551–1562. [[CrossRef](#)]
19. Guo, M.; Liu, K.; Sun, J.; Gu, D. Effects of Laser Scan Strategies on Densification, Residual Stress, and Mechanical Properties of W-Ti Heavy Alloy Fabricated by Laser Powder Bed Fusion. *Chin. J. Lasers* **2023**, *50*, 29–39.
20. Pushp, P.; Dasharath, S.M.; Arati, C. Classification and applications of titanium and its alloys. *Mater. Today Proc.* **2022**, *54*, 537–542. [[CrossRef](#)]
21. Jing, L.L.; Cheng, K.W.; Wang, F.; Shi, J.W. Application of Selective Laser Melting Technology Based on Titanium Alloy in Aerospace Products. *IOP Conf. Ser. Mater. Sci. Eng.* **2020**, *740*, 012056. [[CrossRef](#)]
22. Gao, M.; Wang, J.; Ren, J.; Hong, Q. Effects of scanning strategies on microstructure and properties of selective laser melted cobalt-chromium alloy. *Laser J.* **2020**, *41*, 133–136.
23. Zong, X.; Wang, L.; Gao, Q.; Liu, W.; Zhou, H. The Effect of Laser Scanning Angle on the Structure and Properties of SLM Forming 316L Stainless Steel. *Appl. Laser* **2021**, *41*, 421–430.
24. Xie, Y.-J.; Yang, H.-C.; Wang, X.-B.; Kuang, C.-J.; Han, W. Effects of laser parameters and scanning strategy on the forming properties of selective laser melting TC11 alloy. *Powder Metall. Ind.* **2018**, *28*, 18–24.
25. Zhou, L.; Sun, J.; Bi, X.; Chen, J.; Chen, W.; Ren, Y.; Niu, Y.; Li, C.; Qiu, W.; Yuan, T. Effect of scanning strategies on the microstructure and mechanical properties of Ti–15Mo alloy fabricated by selective laser melting. *Vacuum* **2022**, *205*, 111454. [[CrossRef](#)]
26. Chang, S.J.; Wei, Z.X. Influences of the scanning strategy on surface roughness in selective laser melting. *Proc. Inst. Mech. Eng. Part B J. Eng. Manuf.* **2020**, *236*, 095440542097811. [[CrossRef](#)]
27. Khorasani, A.; Gibson, I.; Awan, U.S.; Ghaderi, A. The Effect of SLM Process Parameters on Density, Hardness, Tensile Strength and Surface Quality of Ti-6Al-4V. *Addit. Manuf.* **2018**, *25*, 176–186. [[CrossRef](#)]
28. Shi, W.; Wang, P.; Liu, Y.; Han, G. Process Strategy of Selected Laser Melting Forming Non-Horizontal Suspension Structure Experiment of Nicochrome Steel. *Chin. J. Rare Met.* **2019**, *43*, 486–493.
29. Wu, G.; Liu, T.; Zhang, C.; Liao, W. Research on Forming Quality of Overhanging Structure by Selective Laser Melting. *China Mech. Eng.* **2016**, *27*, 1810–1815.
30. Wu, G. *Research on Laser Selective Melting Forming Process of Metal Hanging Feature Structure*; Nanjing University of Science and Technology: Nanjing, China, 2016.
31. Yu, W.-Y.; Xiao, Z.-Y.; Cheng, Y.-W.; Chen, Y.-Y.; Gao, C.-F.; Zhang, W.-W. Effect of sloping angle on forming of CoCrMoW alloy by selective laser melting. *Chin. J. Nonferrous Met.* **2017**, *27*, 2251–2259.
32. Weiyong, Y.; Zhiyu, X.; Yingying, C.; Chuanshou, H.; Quanli, Z. Powder Characteristics and Selective Laser Melting Forming Properties of CoCrMoW Alloy. *Rare Met. Mater. Eng.* **2019**, *48*, 973–980.

Disclaimer/Publisher’s Note: The statements, opinions and data contained in all publications are solely those of the individual author(s) and contributor(s) and not of MDPI and/or the editor(s). MDPI and/or the editor(s) disclaim responsibility for any injury to people or property resulting from any ideas, methods, instructions or products referred to in the content.